


# Accurate hypocentre determination in the seismogenic zone of the subducting Nazca Plate in northern Chile using a combined on-/offshore network

**Journal Article****Author(s):**

Husen, S.; Kissling, Eduard ; Flueh, E.; Asch, G.

**Publication date:**

1999

**Permanent link:**

<https://doi.org/10.3929/ethz-b-000422693>

**Rights / license:**

[In Copyright - Non-Commercial Use Permitted](#)

**Originally published in:**

Gheophysical Journal International 138(3), <https://doi.org/10.1046/j.1365-246x.1999.00893.x>

# Accurate hypocentre determination in the seismogenic zone of the subducting Nazca Plate in northern Chile using a combined on-/offshore network

S. Husen,<sup>1,\*</sup> E. Kissling,<sup>2</sup> E. Flueh<sup>1</sup> and G. Asch<sup>3</sup>

<sup>1</sup> GEOMAR Research Center for Marine Sciences of the Christian Albrechts University, Wischhofstrasse 1–3, D 24148 Kiel, Germany.

E-mail: shusen@geomar.de

<sup>2</sup> Institute of Geophysics, ETH-Hönggerberg, Zurich, Switzerland

<sup>3</sup> GeoForschungsZentrum (GFZ), Department 4, Potsdam, Germany

Accepted 1999 March 31. Received 1999 March 29; in original form 1998 June 18

## SUMMARY

The coupled plate interface of subduction zones—commonly called the seismogenic zone—has been recognized as the origin of fatal earthquakes. A subset of the aftershock series of the great Antofagasta thrust-type event (1995 July 30;  $M_w = 8.0$ ) has been used to study the extent of the seismogenic zone in northern Chile. To achieve reliable and precise hypocentre locations we applied the concept of the minimum 1-D model, which incorporates iterative simultaneous inversion of velocity and hypocentre parameters. The minimum 1-D model is complemented by station corrections which are influenced by near-surface velocity heterogeneity and by the individual station elevations. By relocating mine blasts, which were not included in the inversion, we obtain absolute location errors of 1 km in epicentre and 2 km in focal depth. A study of the resolution parameters ALE and DSPR documents the importance of offshore stations on location accuracy for offshore events. Based on precisely determined hypocentres we calculate a depth of 46 km for the lower limit of the seismogenic zone, which is in good agreement with previous studies for this area. For the upper limit we found a depth of 20 km. Our results of an aseismic zone between the upper limit of the seismogenic zone and the surface correlates with a detachment zone proposed by other studies; the results are also in agreement with thermal studies for the Antofagasta forearc region.

**Key words:** aftershocks, earthquake location, seismic tomography, subduction.

## INTRODUCTION

Most of the world's seismicity occurs along subduction zones, and most of the largest earthquakes are generated along these active margins. A closer look reveals that the very largest ones are events mainly of thrust type located within the coupled plate interface at a depth of less than 50 km (Ruff 1996). This part of the subduction zone—commonly called the seismogenic zone—represents a zone where coupling occurs between the downgoing and the overriding plate. At greater depth, the stress regime changes from compressional to extensional stress. The underlying plate tectonic mechanisms are still being debated and depend, among other things, on the extent of the seismogenic zone, specifically the minimum and maximum depths (up-dip and down-dip limits) of this zone (Tichelaar & Ruff 1993; Pacheco *et al.* 1993; Ruff & Tichelaar 1996). A number

of authors have suggested that temperature may control the upper and lower limits of the seismogenic zone (Tichelaar & Ruff 1993; Hyndman & Wang 1995 and references therein). They proposed a temperature of 250 °C to 450 °C as a limit for great earthquake fault slip. A minimum temperature for initiating earthquakes is defined at 100–150 °C (Hyndman & Wang 1995), when stable sliding clays dehydrate to illite and chlorite which are more frictionally unstable.

To determine the minimum and maximum depths of the coupled plate interface, accurate and reliable hypocentre determinations are needed, recorded either teleseismically or by a local network. Global studies based on teleseismic data sets from various subduction zones (Tichelaar & Ruff 1993 and Pacheco *et al.* 1993) reveal a depth range of 35–70 km for the transition zone from unstable to stable sliding along the plate interface, which defines the base of the seismogenic zone. The studies failed, however, to determine the minimum depth of the transition zone, because focal depths of shallow

\*Now at: Institute of Geophysics, ETH-Hönggerberg, Zürich, Switzerland.

events recorded teleseismically strongly depend on an accurate knowledge of bathymetry and/or the properties of the uppermost sedimentary layers (Wiens 1989). On the other hand, local networks provide accurate hypocentre locations (e.g. Maurer & Kradolfer 1996) if additional ocean-bottom seismometers are included, since the upper limit of the seismogenic zone is normally located somewhere between the trench and the coastline (Byrne *et al.* 1988).

In this paper we present the results of a study on the aftershock series of the great  $M_w = 8.0$  Antofagasta underthrust event (Delouis *et al.* 1997). The aftershocks were recorded by a combined on- and offshore network which was part of the interdisciplinary CINCA<sup>1</sup> project. Accurate and reliable hypocentres were achieved by applying the concept of the minimum 1-D model (Kissling 1988; Kissling *et al.* 1994). This approach incorporates iterative simultaneous inversion of hypocentres and 1-D seismic  $P$ - and  $S$ -wave velocity models and thus accounts for the strong coupling between hypocentres and seismic velocities. The highly accurate hypocentres are used to estimate the upper and lower limits of the seismogenic zone for the Antofagasta area.

### The CINCA Seismic Network

The CINCA Seismic Network was planned and carried out by the SFB 267<sup>2</sup>. It was a continuation of the PISCO'94<sup>3</sup> experiment to the west (Asch *et al.* 1994). As part of the CINCA project it was planned to monitor the seismicity in an area around the city of Antofagasta over a three-month period (August–September 1995). The network was originally designed to consist of 22 PDAS recorders with 1 Hz three-component seismometers. The situation changed when, 10 days before the experiment started, a magnitude  $M_w = 8.0$  earthquake (Delouis *et al.* 1997) struck the area around the city of Antofagasta on 1995 July 30. Owing to the expected aftershock series, the German Task Force for Earthquakes of the GFZ Potsdam decided to install an additional 13 REFTEK recorders, so that an average of 35 stations were operating throughout the experiment. The network was maintained by the GeoForschungsZentrum (GFZ) Potsdam and the Free University of Berlin (FUB). Nine ocean-bottom hydrophones (OBHs) complemented the network offshore over a period of 28 days. The OBHs were deployed and recovered by GEOMAR using the research vessel SONNE in two legs of 15 and 13 days each.

Land stations were placed along the coast within the Coastal Cordillera and the Longitudinal Valley (Fig. 1). The Coastal Cordillera represents the remnants of the former Jurassic volcanic arc, which has migrated 300 km to the east since its formation (Scheuber *et al.* 1994). The OBHs were deployed offshore on the continental slope between trench and coastline. In total, the network covers an area of 340 km by 210 km.

All onshore recording sites were equipped with three-component seismometers (MARK L4–3D, 1 Hz), and each channel was recorded at 100 Hz sample frequency. Because there is no way to check if a signal has been observed

simultaneously at different stations, all stations were run in continuous mode. The OBH also recorded with a sample frequency of 100 Hz.

Phase data were stored on CDROM, and routine phase picking and localization of the events were performed with the PITSAs-based package GIANT (Rietbrock & Scherbaum 1998). Since all stations were operated in continuous mode, intensive preprocessing of the raw data was required. A total number of 15 653 events were detected for the three-month period of the CINCA experiment using a software trigger with a LTA to STA ratio of 8 and a coincidence check with at least five stations (Asch *et al.* 1995). To decrease the number of earthquakes to a practical size and to select the most useful events, we increased the requested minimum number of stations per event to 15, thus further reducing the data set to 4426 events. Since we intend to achieve accurate hypocentre locations for offshore events, we use a subset of those 1650 events that were recorded during the period of OBH operation. Preliminary hypocentre locations for this period of 28 days are shown in Fig. 2. During phase picking, the event's local magnitude  $M_L$  was determined by averaging the maximum peak-to-peak amplitude on one of the horizontal components for all available observations. For the subset of 1650 events, local magnitudes range from 0.7 to 5.85 with an average of 2.37.

## ACCURATE HYPOCENTRE LOCATIONS

### The coupled hypocentre velocity problem

The traveltime of a seismic wave is a non-linear function of both the hypocentral parameters and seismic velocities sampled along the ray paths between stations and hypocentre. This dependence on hypocentral parameters and seismic velocities is called the coupled hypocentre–velocity model problem (Crosson 1976; Kissling 1988; Thurber 1992). It can be linearized and written in matrix notation as (Kissling *et al.* 1994)

$$\mathbf{t} = \mathbf{H} + \mathbf{M}\mathbf{m} + \mathbf{e} = \mathbf{A}\mathbf{d} + \mathbf{e}, \quad (1)$$

where  $\mathbf{t}$  is the vector of traveltime residuals (differences between observed and calculated traveltimes);  $\mathbf{H}$  is the matrix of partial derivatives of traveltime with respect to hypocentral parameters;  $\mathbf{h}$  is the vector of hypocentral parameter adjustments;  $\mathbf{M}$  is the matrix of partial derivatives of traveltimes with respect to model parameters;  $\mathbf{m}$  is the vector of velocity parameter adjustments;  $\mathbf{e}$  is the vector of traveltime errors, including contributions from errors in measuring the observed traveltimes, errors in the calculated traveltimes due to errors in station coordinates, use of the wrong velocity model and hypocentral parameters, and errors caused by the linear approximation;  $\mathbf{A}$  is the matrix of all partial derivatives; and  $\mathbf{d}$  is the vector of hypocentral and model parameter adjustments.

In standard earthquake localization, the velocity parameters are kept fixed to *a priori* values—which are assumed to be correct—and the observed traveltimes are minimized by perturbing hypocentral parameters. Neglecting the coupling between hypocentral and velocity parameters during the location process, however, can introduce systematic errors (Thurber 1992; Eberhart-Phillips & Michael 1993) in the hypocentre location. Furthermore, error estimates strongly depend on the assumed *a priori* velocity structure (Kissling *et al.*

<sup>1</sup>Crustal Investigations on- and offshore Nazca plate and Central Andes.

<sup>2</sup>Collaborative Research Group 267, Deformation processes in the Andes.

<sup>3</sup>Proyecto de Investigacion Sismologica de la Cordillera Occidental.

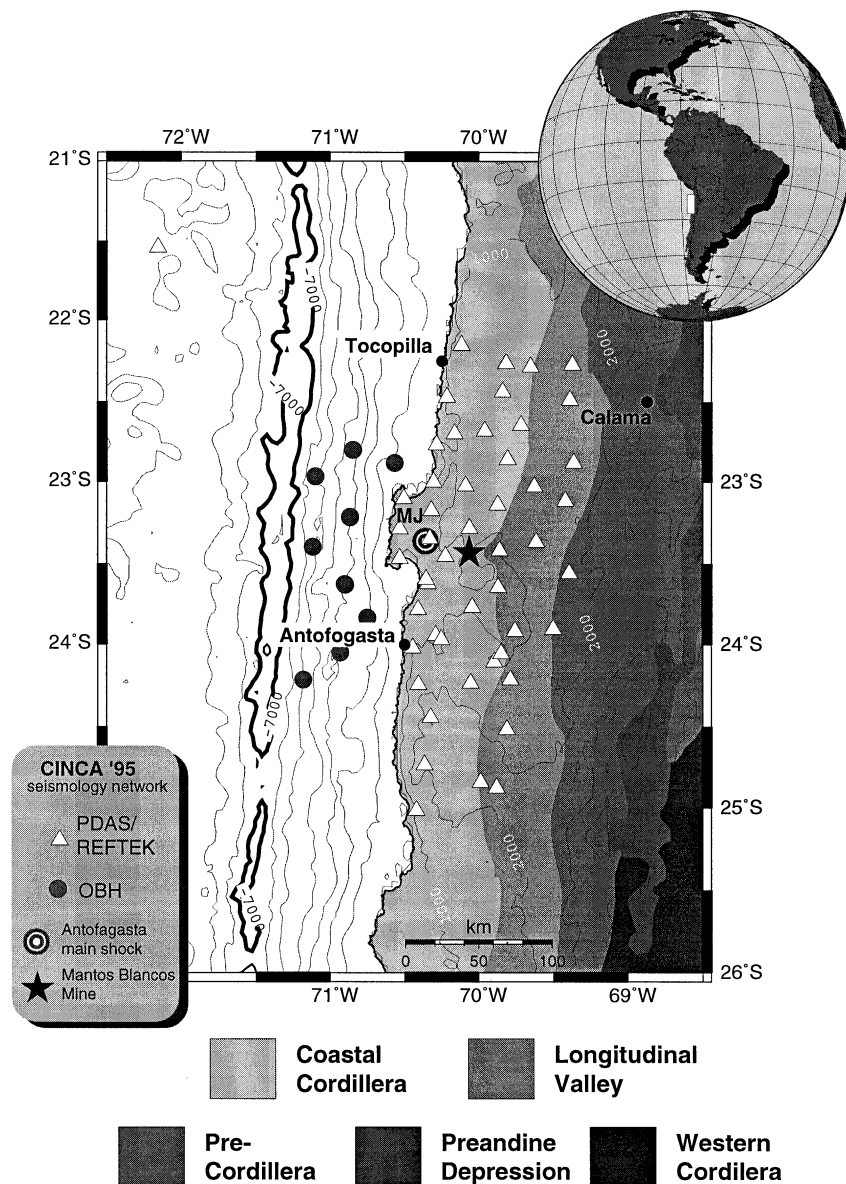
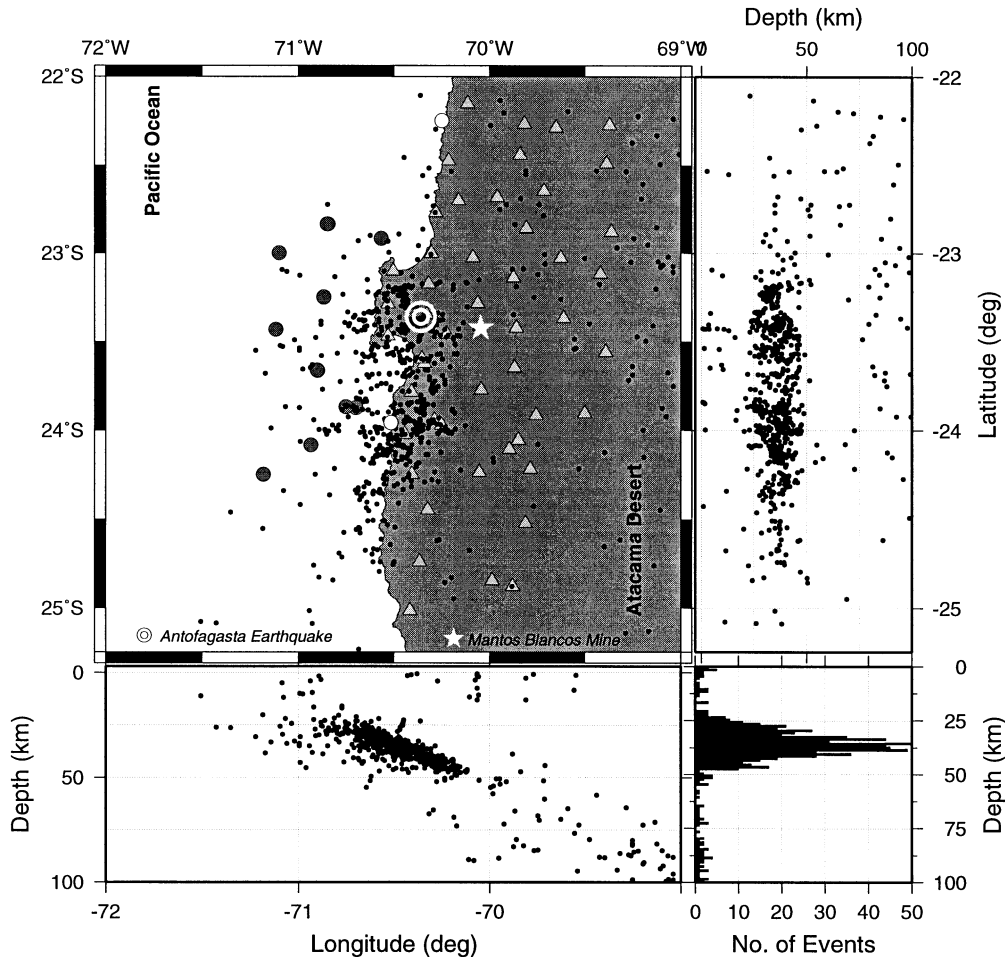


Figure 1. Network design of the CINCA experiment with main geomorphological units (MJ: Mejillones Peninsula). The contour interval of topography is 1000 m. The Trench is marked by the -7000 m isoline. The epicentre of the Antofagasta main shock is taken from the NEIC catalogue.

1995b). Precise hypocentre locations and error estimations therefore demand the solution of all unknowns in the coupled inverse problem, namely the hypocentral parameters and the velocity field. In the minimum 1-D model this will be achieved by simultaneously inverting for hypocentre and velocity parameters (Kissling 1988). The minimum 1-D velocity model obtained by this trial-and-error process represents the velocity model that most closely reflects the *a priori* information obtained by other studies, for example refraction studies, and that leads to a minimum average of RMS values for all earthquakes (Kissling *et al.* 1995b). Each layer velocity of the minimum 1-D model is the weighted area-wise average over all rays in the data set within that depth interval. To account for lateral variations in the shallow subsurface, station corrections are incorporated in the inversion process. For stations with an even azimuthal ray distribution, that is to say in the middle of the network, the station corrections will reflect the near-surface

geology. As a result of the mostly long ray paths and limited azimuthal ray distribution, station corrections in the outer regions of the network contain velocity information about the shallow subsurface and linear effects of the deep structure. The applicability of the concept of the minimum 1-D model even in areas of significant Moho topography and dipping structures, and its performance for high-precision earthquake location have been tested and documented by relocating shots and mine blasts (Kissling 1988; Kradolfer 1989; Kissling & Lahr 1991; Solarino *et al.* 1997). In addition, no significant and systematic shift in hypocentre locations is observed after a 3-D inversion when using the minimum 1-D model as the initial reference model (Kissling 1988; Kissling & Lahr 1991; Graeber 1997). Thus, the minimum 1-D model concept is the most appropriate for uniform high-precision earthquake localization in the CINCA experiment, outperforming any 2-D or 3-D velocity model based on *a priori* information.



**Figure 2.** Seismicity over a one-month period as observed by the CINCA network extended offshore with OBHs. Events have been located routinely using a preliminary velocity model. The white star marks the position of the Mantos Blancos Mine, blasts from which will be used for determining location accuracy.

#### Minimum 1-D velocity model for the CINCA experiment

Data quality is of great importance for the success, efficiency, and accuracy of an inversion process. To establish a set of events that can be accurately located, we select only those events out of the presently available set of some 1650 earthquakes (Fig. 2) that have an azimuthal gap of observations (GAP) of less than  $180^\circ$  and at least 10  $P$  observations. This reduces the data set used for the  $P$ -wave inversion to a total number of 600 events.

The calculation of a minimum 1-D model is a trial and error process starting with a wide range of realistic and possible unrealistic velocities as initial guesses. The use of a wide range of velocities guarantees that all possible solutions are taken into account. The software routine VELEST (Kissling *et al.* 1995a) used for the calculation of the minimum 1-D model allows for station elevation, which implies that the rays are traced exactly to the true elevation position during the forward modelling. This is an important constraint for the CINCA experiment, where we encounter stations at elevations of 2200 m above sea level to 5500 m below sea level yielding a station topography of nearly 8 km. Since the ray tracer currently implemented in VELEST demands that all stations must be located within the first layer, the velocity models in Fig. 3 show a thickness of 8 km for the uppermost layer.

This unusually large thickness of the top layer, however, introduces instabilities into the inversion procedure. In Fig. 3, velocity models as obtained by the inversion are represented by bold lines, and the initial models are plotted with grey lines. Even at intermediate depth, where good resolution is expected because of adequate ray coverage, no convergence among the final velocity models can be observed. Since the first kilometres within the earth crust generally show a strong velocity gradient, an unrealistic thick top layer with a constant velocity as required by VELEST may introduce a systematic error, which would explain the observed instabilities. In an alternative approach, we neglected the station elevations and were thus able to use a more detailed velocity discrimination in the upper layers. The omission of station elevations will, however, result in a systematic 'error' for the calculated traveltimes. For well-locatable events such as those in our selected data set, however, these systematic errors will primarily affect the station corrections (Kissling *et al.* 1994; Maurer & Kradolfer 1996). Differences in ray paths are negligible if focal depths of events are much larger than station elevations and in areas of strong vertical velocity gradient, because rays travel nearly vertically beneath the stations. Station corrections in such a minimum 1-D model, however, include the effects both of station elevations and of local subsurface velocity.

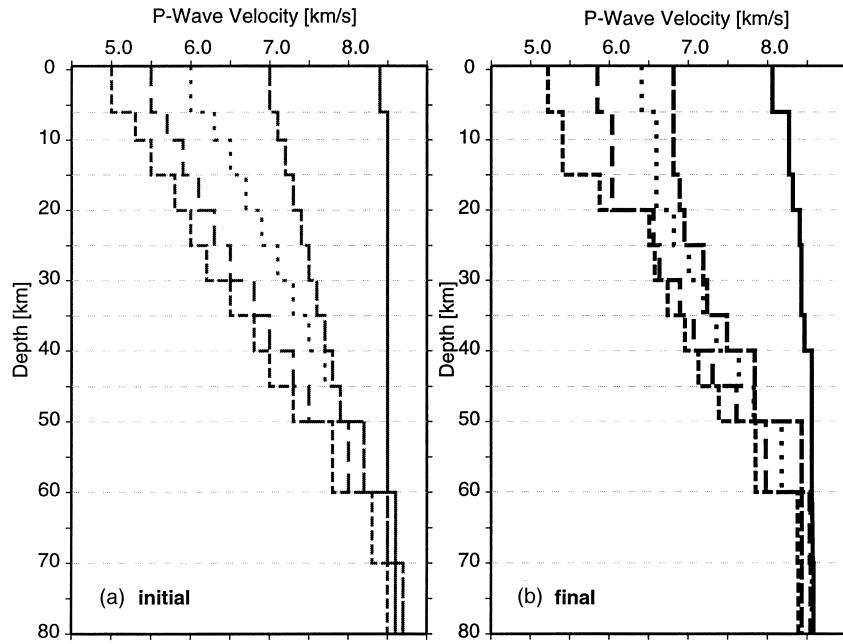


Figure 3. Initial (a) and final (b) 1-D velocity models after inversion with station elevations. Note the poor convergence of the velocity models due to the large thickness of the top layer.

Fig. 4 shows various velocity models with refined upper layer thickness. Initial models are represented by grey lines (Fig. 4a), and final velocities by bold lines (Fig. 4b). The new results—without using the station elevations—show a more consistent behaviour. Below 15 km depth we observe a good convergence among the final velocity models (Fig. 4b). The results for the layers above 10 km depth (Fig. 4b) illustrate the problem in resolving absolute velocities within this depth range as a consequence of the—for this purpose—unfavourable hypocentre–depth distribution.

Owing to intrinsic ambiguities of the inverse coupled hypocentre–velocity problem, additional boundary conditions are needed to select a specific velocity model. In the area around Antofagasta, a refraction profile along the Coastal Cordillera was interpreted by Wigger *et al.* (1994). Since most of the selected earthquakes are located beneath the Coastal Cordillera we may expect the minimum 1-D model velocities to correspond to those velocities obtained by the refraction profile, assuming this refraction model to be representative for the region. Both the minimum 1-D model and refraction model

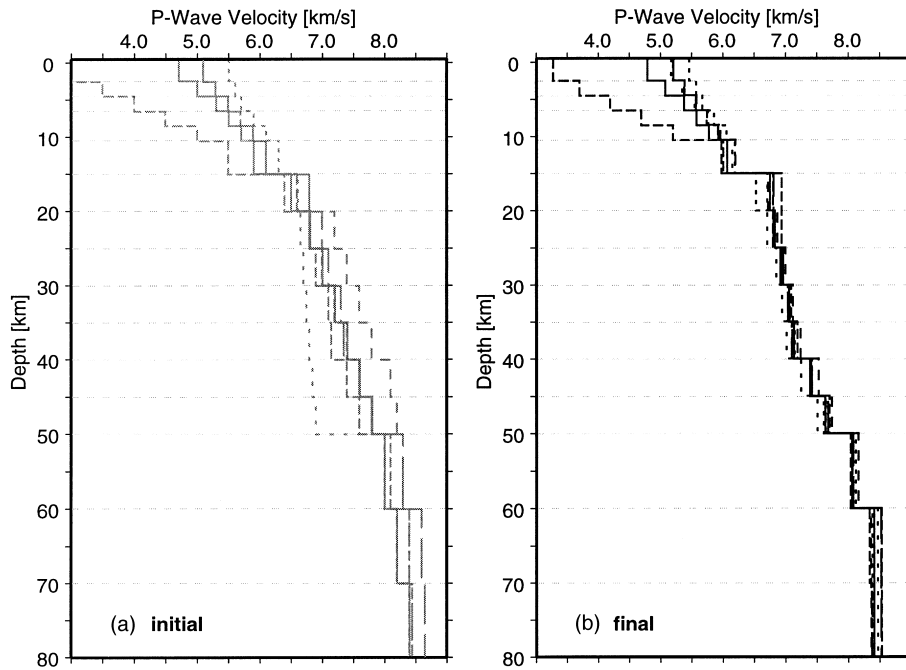


Figure 4. Initial (a) and final (b) 1-D velocity models after inversion with refined upper layer thickness. Above 10 km depth only the velocity gradient can be resolved, not absolute velocities. Below 15 km depth the models converge to an average velocity model.

start with high velocities near the surface and show a moderate gradient in the first 10 km. A strong increase in velocity exists at 15 km depth for the minimum 1-D model (Fig. 6, Table 1). In the refraction profile this contrast is located at 15–20 km and interpreted as the lower boundary of the former Jurassic arc (Wigger *et al.* 1994). The lower crust is represented in both models by high velocities up to  $7.4 \text{ km s}^{-1}$ . Sub-Moho velocities of  $8.3$  and  $8.05 \text{ km s}^{-1}$  are respectively found below 43 km depth in the refraction profile and 50 km depth in the minimum 1-D model.

The *P*-wave station corrections (Fig. 5) show a clear trend from negative values in the west to positive values in the east. This trend is mainly caused by high velocities within the subducting oceanic plate dipping to the east. Waves from deep events in the eastern part travelling up-dip along this high-velocity anomaly on their way to the OBH are faster than those calculated for the 1-D velocity model, which results in negative traveltime residuals. Down-dip ray paths through the subducting oceanic plate and low near-surface velocities due to sediment coverage of the Longitudinal Valley are responsible for the observed positive station corrections of stations on land in the eastern part of the network.

### Minimum 1-D *S*-velocity model

*S*-wave phases add important additional constraints on hypocentre locations. Gomberg *et al.* (1990) demonstrated that partial derivatives of *S*-wave traveltimes are always larger than those of *P* waves by a factor equivalent to  $V_p/V_s$  and that they act as a unique constraint within an epicentral distance of 1.4 focal depths. The use of *S* waves will in general result in a more accurate hypocentre location, especially regarding focal depth.

On the other hand, a mispicked *S* arrival time at a station close to the epicentre can result in a stable solution with a small RMS, but that actually denotes a significantly mislocated hypocentre even for cases with excellent azimuthal station coverage. Since the onset of *S* phases is often masked or distorted by *P*-wave coda, mispicking is more likely to occur with *S* phases, and a critical quality control is needed. To reduce the possibility of mispicked *S* arrival times we rotate and integrate the horizontal components before picking. After phase picking, we relocate all events with a consistent-velocity model and select only those events with a  $\text{GAP} < 180^\circ$  and with at least 10 good *P* and five good *S* phases. To check

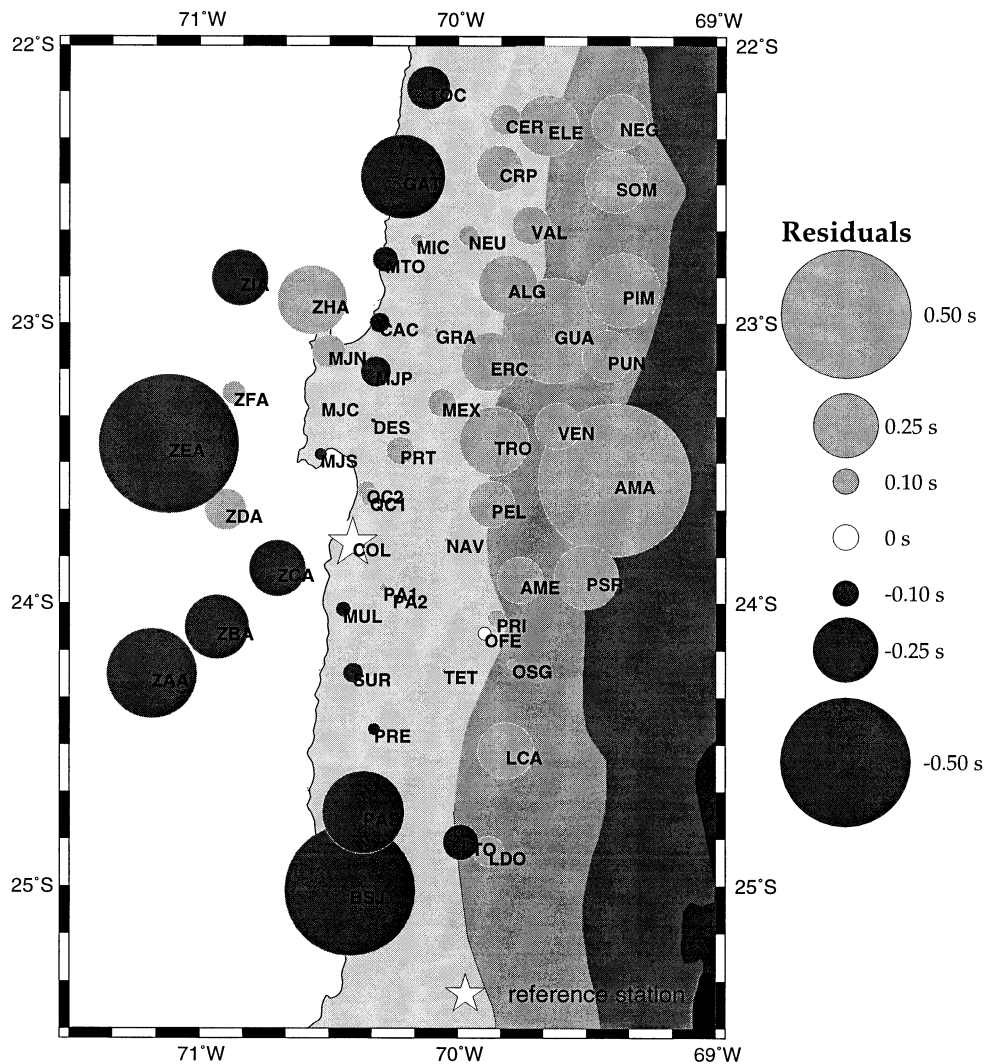


**Figure 5.** Final *P*-wave station corrections for the minimum 1-D velocity model. The reference station (COL) is marked by a white star. For further discussion see text.

for data blunders we plot histograms of the residuals sorted by observation weight and eliminate data with exceptional residuals. A final check includes plotting  $P$ -arrivals and  $S$ - $P$  arrivals in a Wadati diagram and eliminating phases lying far off the main trend. The final data set for the  $P$ - and  $S$ -wave inversion consists of 560 events with 12 574  $P$  and 7429  $S$  phases.

In general,  $S$  phases are included in the location procedure by simply assuming a constant  $V_p/V_s$  ratio. By synthetic testing, Maurer & Kradolfer (1996) showed that focal-depth errors obtained with a fixed  $V_p/V_s$  ratio are nearly twice as large as the errors using  $P$ -phases only. The use of an independent  $S$ -wave velocity yielded the best results. Consequently, we determined a minimum 1-D  $S$ -wave velocity model by an additional series of inversions.

Four different  $V_p/V_s$  values ranging from 1.6 to 1.9 were chosen to construct four initial  $S$ -wave velocity models for the joint  $P$ - and  $S$ -wave velocity inversion (Fig. 6). In each case, the previously calculated minimum 1-D  $P$ -velocity model with corresponding station corrections was taken as the initial  $P$ -wave velocity model. Equal damping of the  $P$ -wave velocities results in unrealistically high  $P$ -wave velocities for the shallow layers where no events are located. For this reason,  $P$ -wave velocities for the topmost 15 km were more or less fixed to the initial values by strong overdamping. Fig. 6 and Table 1 show the final  $P$ - and  $S$ -wave velocities and the corresponding  $V_p/V_s$  ratio for the various initial models. For depths shallower than 15 km, the  $V_p/V_s$  ratio is close to the initial value.  $V_p/V_s$  ratios diverge below 60 km depth for all models, a phenomenon that was found to be a result of the low number of events within this depth range.

**Table 1.**  $P$ -wave and  $S$ -wave velocities and resulting  $V_p/V_s$  ratio of the minimum 1-D velocity model.

Depth (km)	$V_p$ (km s <sup>-1</sup> )	$V_s$ (km s <sup>-1</sup> )	$V_p/V_s$
-0.50	5.21	2.99	1.74
2.50	5.37	3.09	1.74
4.50	5.55	3.19	1.74
6.50	5.72	3.29	1.74
8.50	5.89	3.39	1.74
10.50	5.98	3.44	1.74
15.00	6.80	3.75	1.81
20.00	6.81	3.88	1.76
25.00	6.95	3.94	1.76
30.00	6.98	4.05	1.72
35.00	7.11	4.11	1.73
40.00	7.41	4.18	1.77
45.00	7.69	4.30	1.79
50.00	8.05	4.39	1.83
60.00	8.48	4.73	1.79
70.00	8.48	4.78	1.77

### Stability of the minimum 1-D model of the Antofagasta area

To test the stability of the final  $P$ - and  $S$ -wave minimum 1-D velocity model we performed various tests with randomly and systematically shifted hypocentres. Shifting the hypocentres randomly in one direction by 10–15 km before introducing them into the joint velocity–hypocentral parameter inversion provides a check for possible small bias in the hypocentre locations and for the stability of the solution to the coupled problem. If the proposed minimum 1-D velocity model denotes

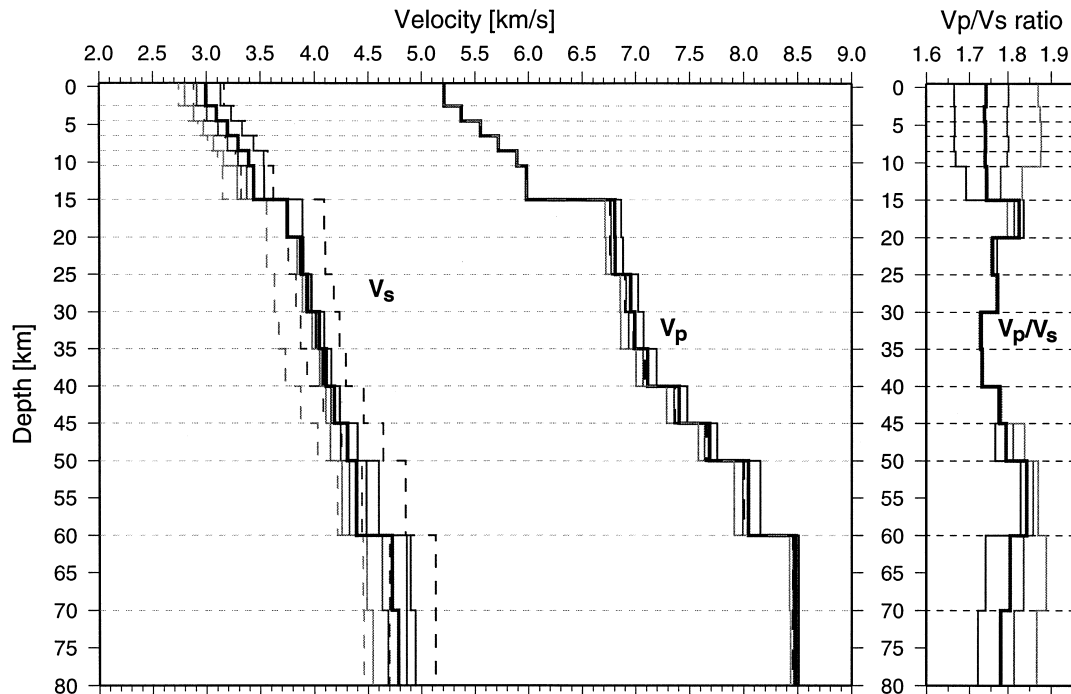


**Figure 6.** Initial (dashed) and final (solid)  $P$ - and  $S$ -wave velocity models. The minimum 1-D  $P$ -wave velocity model has been taken for all models as the initial  $P$ -wave model. The initial  $S$ -wave velocities were calculated using various  $V_p/V_s$  ratios as noted in the plot.  $P$ -wave velocities were fixed for all models to a depth of 15 km because of the poor resolution within these layers. The final  $V_p/V_s$  ratios after the 1-D inversion are displayed on the right. The chosen minimum 1-D  $P$ - and  $S$ -wave velocity model is marked by the bold line. Velocity values are listed in Table 1.



a robust minimum in the solution space, no significant changes in velocity and hypocentre locations are to be expected. Fig. 7 displays the difference in focal depth, latitude, and longitude between the original hypocentres (as obtained by independent *P*- and *S*-wave inversion) and the hypocentres that are randomly shifted by 10–15 km before being introduced into the inversion. All events are relocated close to their original position, demonstrating that the hypocentre locations obtained by the inversion process are not systematically biased.

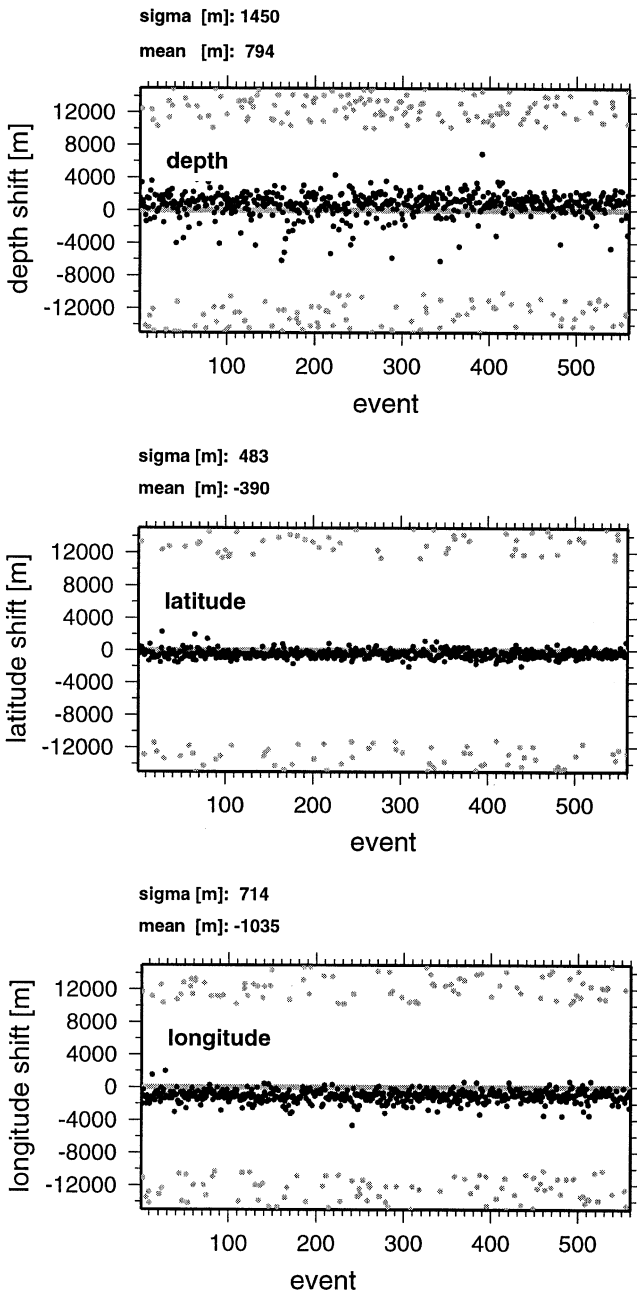


**Figure 7.** Mislocation of hypocentres randomly shifted by 10 to 15 km before being introduced into the 1-D *P*+*S* inversion using the minimum 1-D *P*+*S* velocity model. Grey dots denote the systematic shift of the hypocentre locations before introducing them into the inversion. All hypocentres are relocated to their original position, indicating that no location bias is present. The relative mislocation error in focal depth is nearly twice that in latitude and longitude, as expressed by the larger sigma value.

The shifting of the hypocentres systematically in one direction, for example focal depth, is a good test for the robustness of a minimum 1-D model. After shifting all events to a greater depth by 10 km, two inversions were performed, one with slightly damped and one with strongly overdamped velocities, the results of which are shown in Figs 8(a) and (b), respectively. Since we solve a coupled hypocentre–velocity problem, the initial bias in the hypocentres may be compensated by adjusting the velocities, or by relocating the events to their original position, or by a combination of these methods. When reducing the degree of freedom by fixing the velocities during the inversion, the hypocentres are relocated relatively close to their original position (Fig. 8b) except for a shift in depth of 3.4 km. The hypocentres remain in their shifted position (Fig. 8a) when we use regular damping in the inversion. In combination with the previous findings regarding the depth of the hypocentres, the small deviations in latitude and longitude for both test cases (Figs 8a and b) indicate a decoupling of the epicentre problem from the velocity and a strong coupling of the depth/origin-time problem to the velocity for our data set.

#### Accuracy of hypocentre locations

The relocation of mine blasts or shots provides a good absolute error estimate for hypocentre locations. To provide independent information for such testing, these data were not included in the previous inversion process. The error expected from this approach will be higher than that of earthquakes at greater depth, because for events located close to the surface the waves travel twice through shallow and heterogeneous structures poorly accounted for by the model (Kissling 1988, his Fig. 14). In the CINCA experiment, near-surface velocities are poorly constrained, because most rays travel nearly vertically at shallow depths due to the unfavourable event-depth distribution. Seven blasts in the Mantos Blancos copper mine situated inside the network were relocated using the minimum 1-D model for *P*- and *S*-wave velocities with corresponding station corrections. The mislocation vectors of the relocated blasts relative to the true mine location are shown in Fig. 9. The diameter of the circle represents the uncertainty of the blasts within the mine. The first relocations (marked by circles in Fig. 9) with the minimum 1-D model result in precise epicentre positions; focal depths, however, show consistently large offsets. This unexpected large deviation in depth could be caused by an inadequate approximation of the local near-surface velocities in the vicinity of the mine. To overcome this problem, we relocate the mine blasts performing a *P*- and *S*-wave inversion with all velocities fixed except those of the first two layers, which are regularly damped. The new positions with adjusted near-surface velocities (marked as stars in Fig. 9) show identical results for the epicentres and a more realistic focal depth. Hence, we estimate an absolute error of 1 km in epicentre location and of 2 km in focal depth.

#### Improvement on hypocentre locations using OBH data

Apart from the applied velocity model, hypocentre locations are also sensitive to the azimuthal distribution of stations observing the event. Since a significant part of the aftershock series is located offshore, the OBHs are of obvious importance in the extension of the seismic network over the seismogenic zone and the improvement of its location capabilities. To

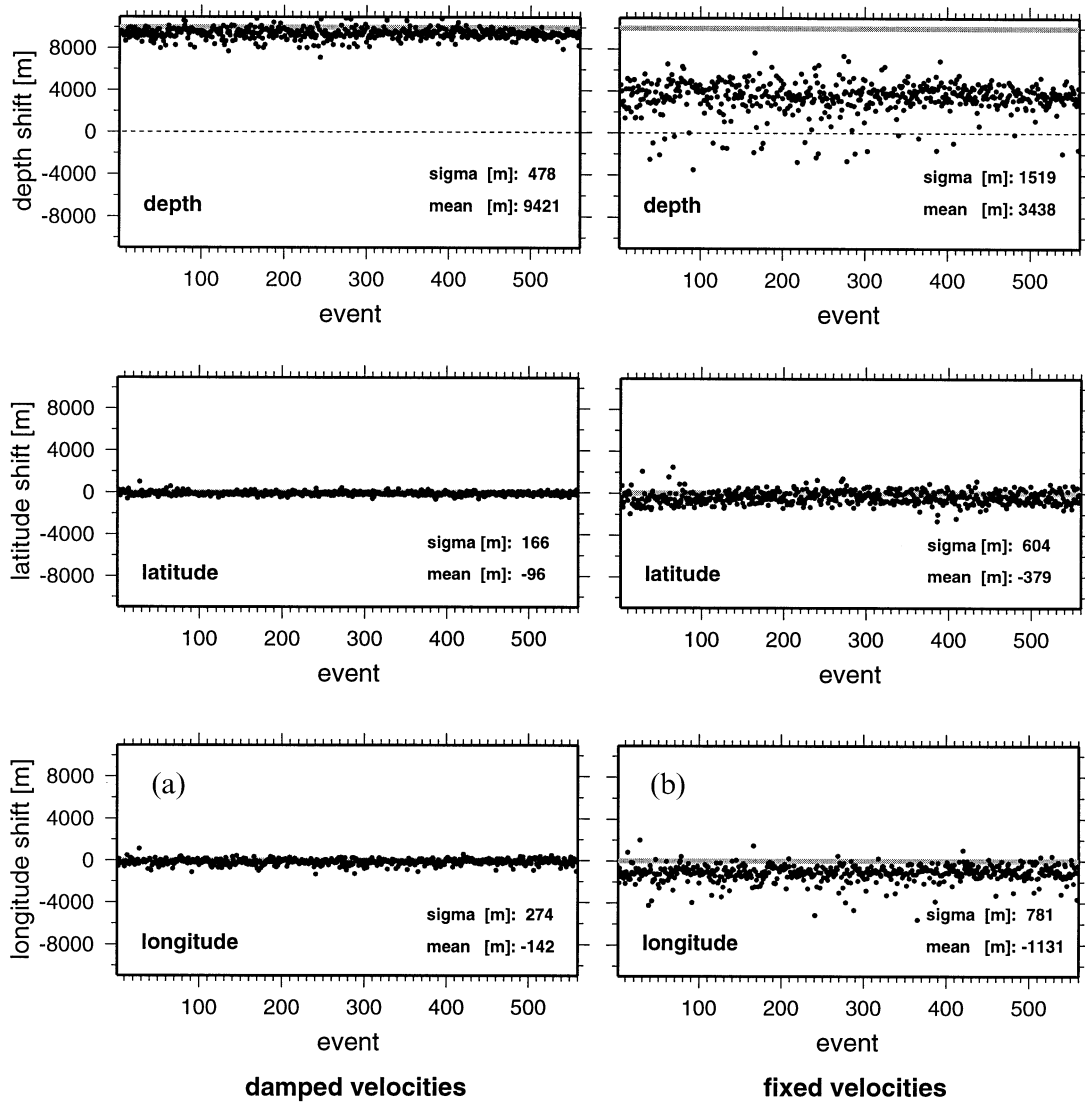


**Figure 8.** (a) Mislocation of hypocentres systematically shifted to greater depth before being introduced into the 1-D  $P + S$  inversion using the minimum 1-D  $P + S$  velocity model. Damping of the velocities prevents a relocation of the hypocentres to their original positions. (b) As (a), but with fixed velocities. Hypocentres are now relocated close to their original positions. Note the weak influence of the shift in depth on latitude and longitude, indicating the decoupling of epicentre and depth/origin-time determination. Grey dots denote the systematic shift of the hypocentre locations before their introduction into the inversion.

investigate the influence of the OBH data on hypocentre locations we established a second minimum 1-D model using only stations on land. An unfavourable distribution of selected earthquakes prevented us from resolving the expected strong variations in the upper crust between the offshore and onshore areas. Hence, the differences between these two minimum 1-D velocity models are small. The changes in the hypocentres discussed below are therefore mainly due to alterations in the geometry of the location problem.

Differences in hypocentre locations of up to 9 km in focal depth and 4 km in epicentre are observed when locating the offshore events with and without OBHs. To demonstrate that these mislocations are due to an unfavourable azimuthal coverage, we computed for each case the resolution matrix for one event. Fig. 10 shows the azimuthal coverage and Table 2 lists the hypocentre locations obtained with and without OBH for this event. Analogous to seismic tomography and other inversion studies, the resolution matrix for the hypocentre

location problem provides an estimate of the interdependence of the resulting hypocentral parameters. For a perfect solution, the corresponding diagonal element is close to one. Table 3 summarizes the resolution diagonal elements for the selected event and for both locations (with/without OBHs). A strong decrease for the diagonal elements corresponding to longitude and focal depth is clearly visible. The first is a response to the lack of stations located to the west of the epicentre when neglecting the OBHs. The lower resolution in focal depth results from the loss of a station within the focal-depth distance. Readings within these distances provide a tighter constraint on the hypocentre location than those with larger offsets (Gomberg *et al.* 1990). Consequently, the poorer resolution in longitude and focal depth for the location without the OBHs is expressed in a large difference in focal depth and longitude between the two locations.

Computing and analysing the resolution matrix for a large set of earthquakes is obviously impractical. RMS values,

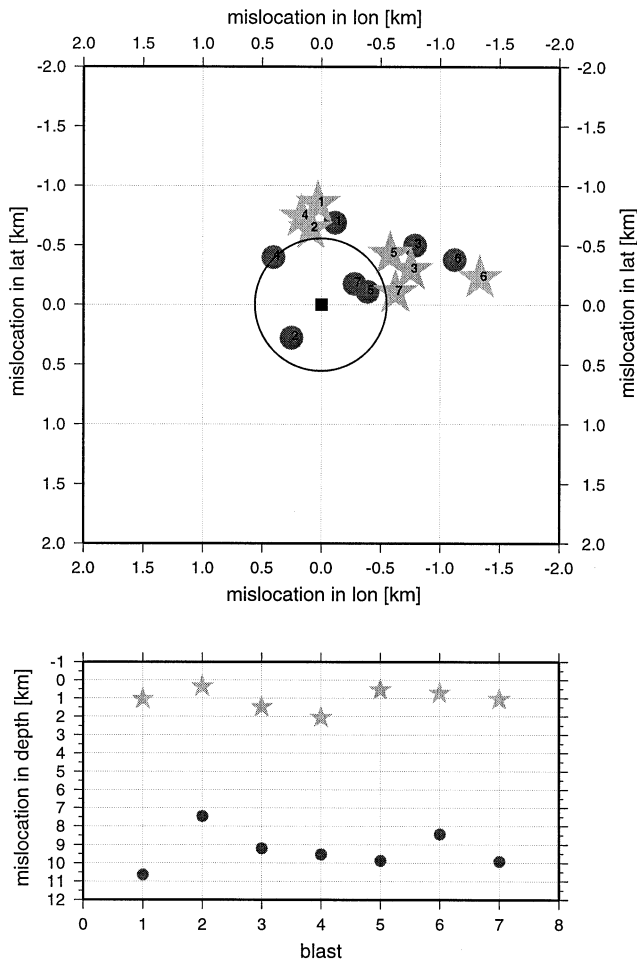


**Figure 9.** Mislocation in epicentre (top) and depth (bottom) of relocated Mantos Blancos blasts. The large offset for the events marked by a circle is due to inadequate approximation of the near-surface velocities of the minimum 1-D model. Adjusting the velocities results in a more realistic depth (marked with stars). Using these relocations, the location error is estimated to 2 km in depth and to 1 km in epicentre.

however, are a poor diagnostic tool for judging the quality of hypocentre solutions. In the test event, we observe a smaller RMS value for the location obtained without using OBHs. This is a consequence of the smaller number of stations for this event, which in general results in a lower RMS estimate. Rather than the RMS value or the full resolution matrix, we propose to use the Dirichlet spread function (DSPR) and the average logarithmic eigenvalue (ALE), which were introduced by Kradolfer (1989). The ALE is based on the eigenvalues of the hypocentre location problem and qualifies the geometry of an earthquake location problem. For an optimal location geometry, the ALE is close to zero. The DSPR is based on the  $L_2$  norm of the difference between the resolution matrix for the problem and an identity matrix (Menke 1984), and describes the goodness of resolution or how well the problem can be solved. For a perfect resolution, the resolution matrix becomes the identity matrix and, consequently, the spread is zero. In Table 2 the ALE and DSPR values are listed for both locations. Both methods give larger values for the hypocentre location obtained without OBHs, and hence, based on the diagnostic tools (ALE and DSPR), one obtains the correct error estimate for the hypocentre locations.

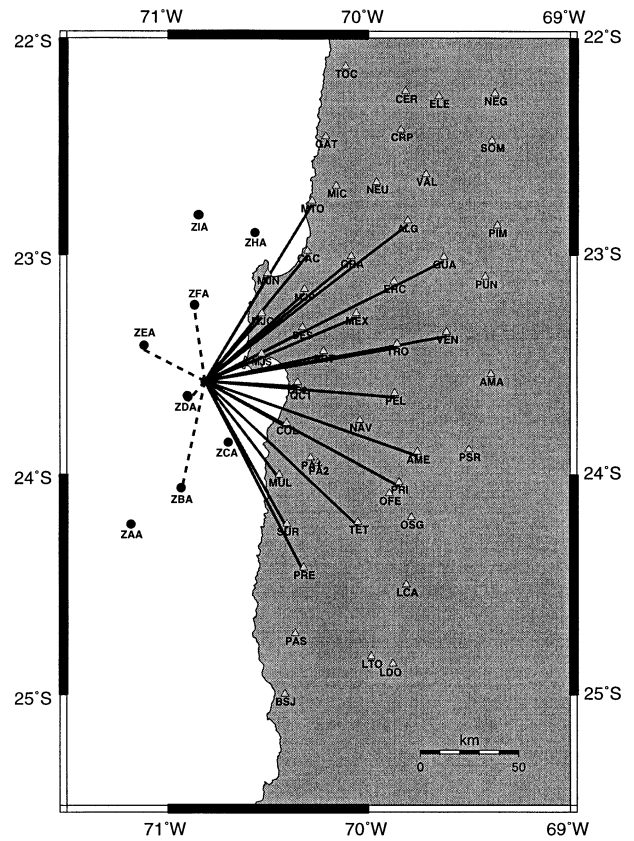


**Figure 10.** Azimuth distribution of recorded stations for an offshore event located with and without OBHs. Details of location accuracy can be found in the text and Tables 2 and 3.

**Table 2.** Statistical parameters for selected events located with and without OBHs.

	with OBH	without OBH
latitude	23.5761°S	23.5704°S
longitude	70.8156°W	70.7855°W
focal depth	14.64 km	23.14 km
no. of phases ( $P + S$ )	34	40
$P_{min}$	13 km	28 km
$S_{min}$	28 km	28 km
GAP	77°	235°
RMS	0.24 s	0.17 s
ALE	1.814	2.166
DSPR	0.025	0.210

ALE and DSPR values for all events located with and without OBH data are displayed in Figs 11 and 12, respectively. Nearly identical results are achieved in the onshore area for the two location problems, indicating the weak influence of OBH data on events located beneath land stations. As expected, large differences exist in the offshore area. As a consequence of the unfavourable azimuthal coverage, ALE and DSPR increase rapidly when the OBH data are not included. Without the use of OBHs, reliable offshore hypocentre determination is therefore restricted to the region within the land station network. Mislocations in focal depth and epicentre of offshore events without the use of OBHs—or in general for events outside the station network ( $GAP < 180^\circ$ )—are up to 9 km in

**Table 3.** Diagonal elements of the resolution matrix located with/without OBH. For further discussion see text.

	origin time	latitude	longitude	depth
origin time	0.9989/0.9952			
latitude		0.9048/0.6842		
longitude			0.9610/0.9507	
depth				0.8975/0.6802

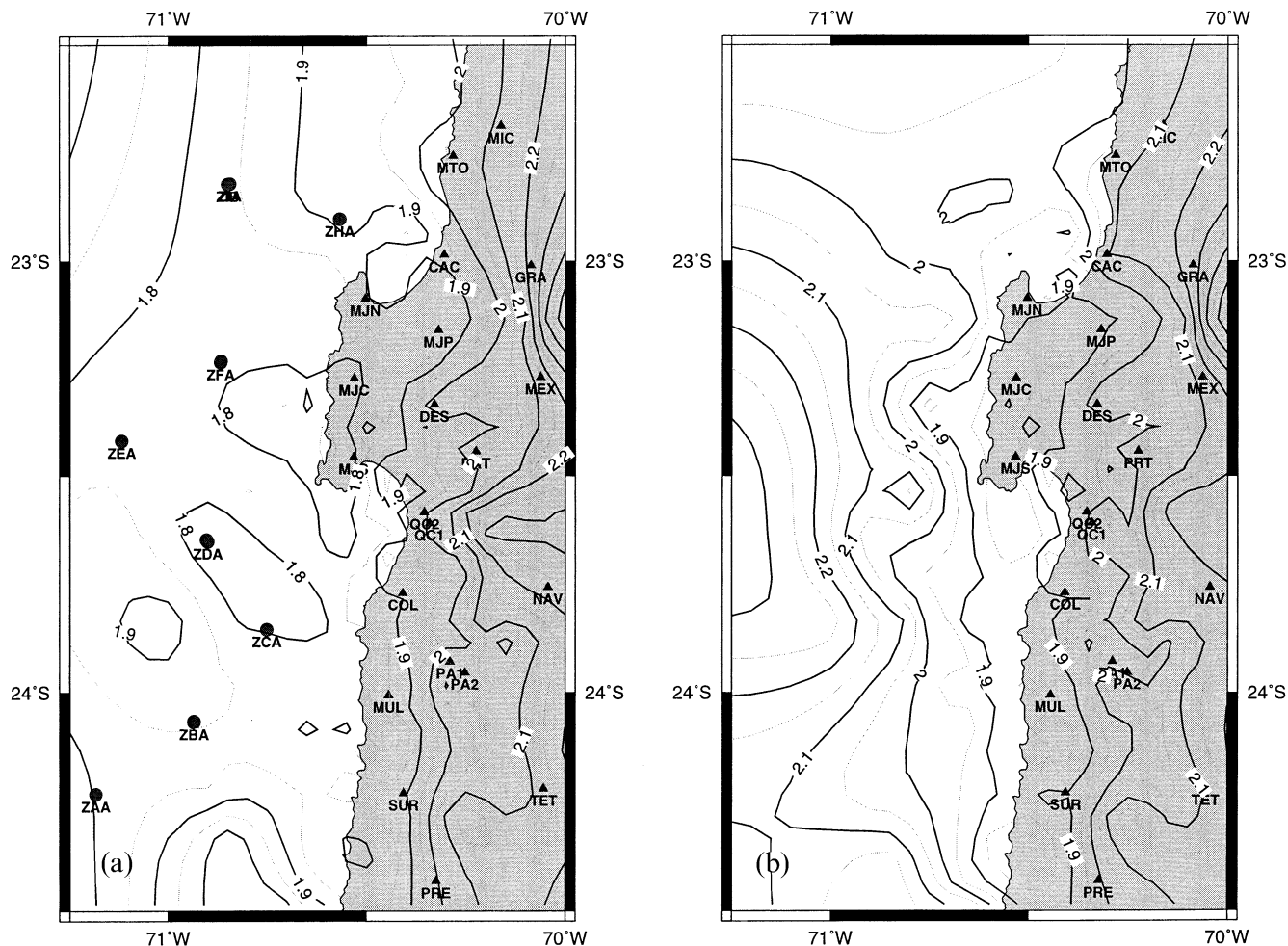


**Figure 11.** (a) Contour lines of ALE values for events located with OBHs. The contour interval is 0.05. (b) As (a), but now all events are located without OBH data. Higher values offshore indicate the poorer geometry of the location problem because of the neglect of the important OBH phases.

focal depth and 4 km in epicentre, which is more than three times the estimated mislocation vector.

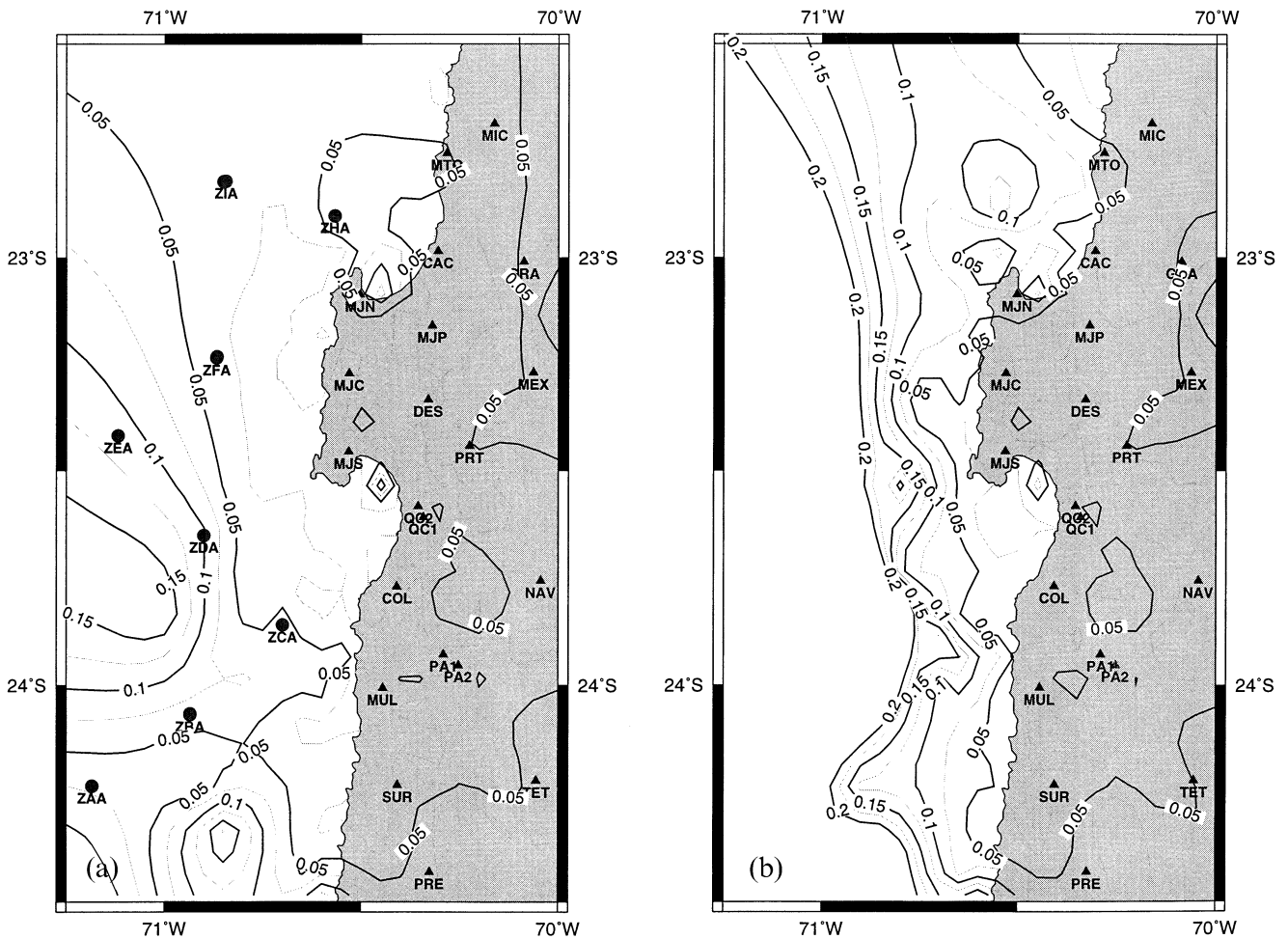
**DISTRIBUTION OF THE ANTOFAGASTA AFTERSHOCKS**

Fig. 13 shows the final hypocentre locations of all 560 well-locatable events used in the *P*- and *S*-wave inversion. A latitudinal depth section is plotted on the right side of the central figure, and a longitudinal depth section is plotted along the bottom. In the lower right corner, the minimum 1-D models for *P*- and *S*-wave velocities are displayed.

The majority of epicentres are concentrated within the rupture area of the main shock as determined by Delouis *et al.* (1997). It seems that within this rupture area two sub-

areas can be identified: one located at the southern tip of the Mejillones Peninsula and one offshore towards the centre of the rupture zone. These two locations coincide with the locations of the two main sources, which released 74 per cent of the total seismic moment (Delouis *et al.* 1997). Besides the aftershock activity, a small amount of background seismicity is observed.

The longitudinal depth section reveals a sharp upper boundary of the Wadati Benioff zone (WBZ), which dips at an average angle of 19°–20° to a depth of 50 km (Fig. 13). This dip corresponds to the estimated dip of the fault-plane solution of the main shock (Delouis *et al.* 1997). Towards the trench, seismicity is low (Fig. 2) and no reliable hypocentres could be determined for these events outside the network. Below 50 km depth and east of 70°W the pattern of seismicity



**Figure 12.** (a) Contour lines of Dirichlet-Spread values for events located with OBHs. The contour interval is 0.025. (b) As (a), but now all events are located without OBH data. The higher values offshore indicate lower resolution. Reliable hypocentres are now limited to a narrow stretch along the coast.

changes remarkably, as observed by other workers (Comte *et al.* 1994; Delouis *et al.* 1996). The sharp upper boundary disappears and the depth distribution becomes irregular. This change probably indicates the maximum depth of the rupture zone and coincides with the transition from a compressional stress regime to a more tensional one (Comte *et al.* 1994; Comte & Suarez 1995; Delouis *et al.* 1996).

During our observation period crustal seismicity was at a very low level, although the area under study shows recent fault activity, mainly of extensional character (Armijo & Thiele 1990; Delouis *et al.* 1998). A cluster of six events was detected in the lower crust at a depth of 21 km, clearly separated from the main activity along the Wadati Benioff zone (Fig. 13). Excellent azimuthal coverage leads to an estimated location error of only 2 km in focal depth for these events. They occurred within one day and show a magnitude of up to 4.0 as determined by the local network. The location of the epicentres suggests a possible relation of these events with the Atacama Fault System, a major zone of deformation that stretches nearly parallel to the coastline at an offset of 30–50 km for about 1100 km (Armijo & Thiele 1990). Deformation observed along the Atacama Fault System is characterized by vertical uplift and subsidence related to normal faulting. Strike-slip components are also observed but with moderate

offsets (Armijo & Thiele 1990; Delouis *et al.* 1998). Preliminary focal mechanism solutions of five events of the cluster show two strike-slip and three mainly normal fault solutions. Since this area is within the rupture zone of the Antofagasta main shock and the clustering of the events happens in space and time, it is likely that the observed crustal activity was triggered by the main shock, but further study is needed to confirm a possible relation to the Atacama Fault System. No events have been detected at shallow crustal levels, which may be due to the high noise level generated by the aftershock activity. On the other hand, no shallow seismicity has been reported by other workers (Comte *et al.* 1994; Delouis *et al.* 1996), in contrast to the fault activity observed at the surface (Armijo & Thiele 1990; Delouis *et al.* 1998).

#### MAXIMUM AND MINIMUM DEPTH OF THE COUPLED SEISMOGENIC ZONE

The extent of the seismogenic zone has been studied by analysing either the distribution of focal mechanisms of the normal seismicity (e.g. Comte *et al.* 1994; Delouis *et al.* 1996) or the aftershock distribution of a great underthrust event within the seismogenic zone (Tichelaar & Ruff 1993). Both approaches complement each other and are needed to define

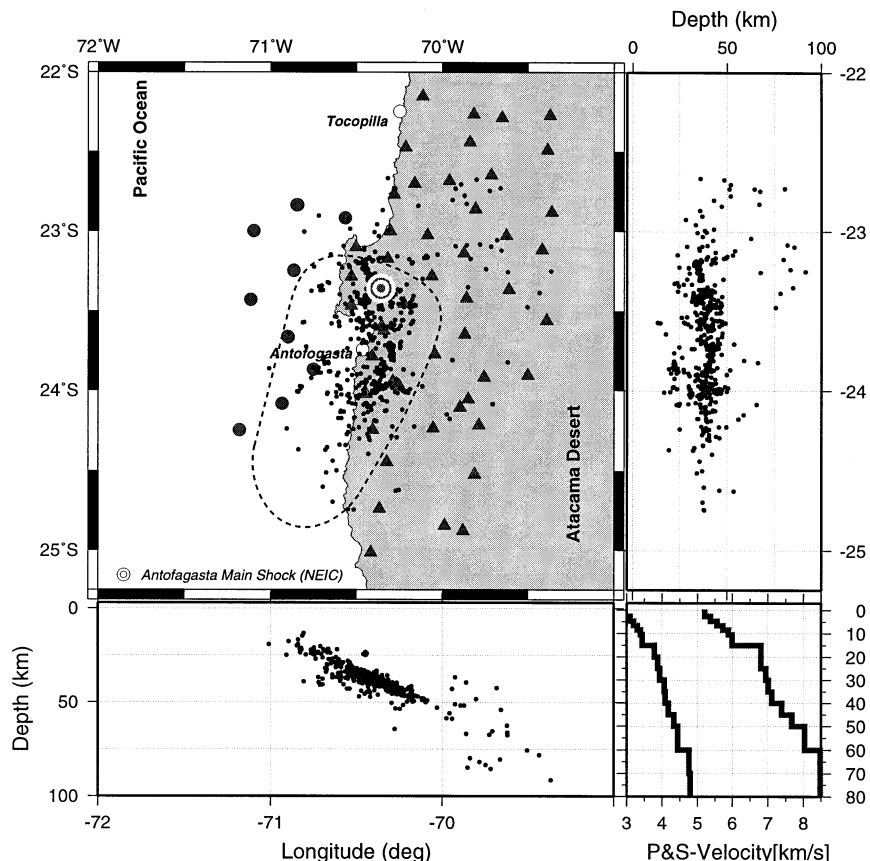


**Figure 13.** Accurate hypocentres as determined by an independent  $P + S$  inversion using a combined on-/offshore network. Vertical depth sections along latitude and longitude are shown at the bottom and right side, respectively. The minimum 1-D velocity model for  $P$ - and  $S$ -waves is displayed on the lower right. The area marked by the dashed line denotes the rupture area of the Antofagasta main shock, after Delouis *et al.* (1997).

clearly the extent of the seismogenic zone within a subducting plate. In general, the determination of the maximum and minimum depths of the seismogenic zone has been based on detailed focal mechanism analysis. Several studies in northern Chile aimed to define the extent of the coupled plate interface. Comte *et al.* (1994) used focal mechanisms of locally recorded earthquakes and found a maximum depth of shallow-dipping thrust events of 47 km in the Antofagasta area. Recently, Delouis *et al.* (1996) performed a simultaneous determination of orientation and shape of the local stress tensor and of individual focal mechanisms using locally recorded earthquakes within the Antofagasta region, and found the lower limit of the coupled plate interface at a depth of 50 km. Tichelaar & Ruff (1991) used focal mechanisms from teleseismically recorded aftershocks of magnitudes greater than 6 for the central and northern part of the Chilean subduction zone. Their results of a maximum depth of 46–48 km for northern Chile are poorly constrained because no large earthquake ruptured this area between 1877 and 1995. None of these earlier studies regarding the extent of the seismogenic zone can provide a reliable value for the minimum depth of the coupled plate interface. The use of teleseismic events at shallow depths in subduction zones relies strongly on the knowledge of bathymetry and/or properties of the uppermost sedimentary layers (Pacheco *et al.* 1993; Wiens 1989). On the other hand, local networks used by Comte *et al.* (1994) and Delouis *et al.* (1996) failed to determine accurate depths for offshore events since their networks were restricted to onshore stations.

Since our analysis of the seismogenic zone is based on the high-precision location of the aftershock series of a great underthrust event, we are able to give reliable estimates for both the minimum and maximum depths of the seismogenic zone. In order to exclude earthquakes located within the subducting oceanic plate from the study, we select only the shallowest event within a specified bin width. Fig. 14 displays

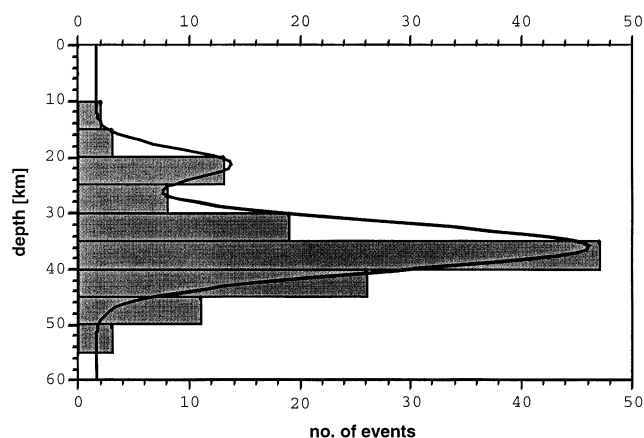


**Figure 14.** Depth distribution of events belonging to the aftershock series. The data have been binned using only the shallowest events in each bin. The distribution could be fitted well by a double Gaussian distribution (see text for more details).

the focal depth distributions of these events. Our data have a good fit to a double Gaussian distribution with depth, although the second maximum is not very dominant. Following Pacheco *et al.* (1993), we define the maximum and minimum depths of the seismogenic zone by the 95th and the 5th percentile, respectively. This approach accounts for uncertainties in depth distribution resulting from location errors and from incompleteness due to the restricted observation period. With this approach we find the maximum depth of the seismogenic zone at a depth of 46 km, which fits well in the range found by Tichelaar & Ruff (1991), Comte & Suarez (1995) and Delouis *et al.* (1996), and the minimum depth at 20 km depth.

Numerical modelling of the temperature field of the coupling interface supports the concept that a critical temperature may play a key role in controlling the extent of the seismogenic zone. A critical temperature of 100–150 °C was found at the upper boundary (Hyndman & Wang 1995) and of 250 °C or 400–550 °C at the lower boundary, depending on the distribution of shear stress at the coupling interface (Tichelaar & Ruff 1993; Hyndman & Wang 1995). Models of the temperature field in the forearc region of the Antofagasta area (Springer 1997) show a temperature of 200–250 °C for a depth of 46 km, corresponding to the maximum depth of the seismogenic zone. Tichelaar & Ruff (1993) pointed out that the distribution of shear stress along the coupling interface is an important parameter for the critical temperature at the lower boundary. Assuming a constant coefficient of friction, they found two critical temperatures of 400 °C and 550 °C. Assuming constant stress with depth, however, they found a single critical temperature of 250 °C. To explain the low values of heat flow observed in the Antofagasta forearc region, Springer (1997) used a constant shear stress for the thermal modelling, thereby explaining the low critical temperature found at the lower boundary of the seismogenic zone.

Byrne *et al.* (1988) recognized that in most subduction zones earthquakes do not extend up-dip along the plate interface all the way to the trench axis or deformation front. They argued that the existence of this aseismic zone is caused by stable slip properties of the unconsolidated and semiconsolidated sediment in that zone. At greater depth the sediment becomes more consolidated and de-watered and comes into contact with harder rocks of the overlying plate. Here the slip behaviour changes to unstable stick-slip sliding accommodated seismically as episodic slip in large earthquakes. Sediments are essentially lacking in the trench axis off northern Chile (Hinz *et al.* 1995), however, and the subduction zone along northern Chile has been characterized as erosional type (von Huene & Scholl 1991). A detachment zone which decouples the converging upper and lower plates and which is only effective seawards of the seismogenic zone (von Huene *et al.* 1998) may be responsible for the observed lack of stronger seismic events at shallow depths. Such a detachment zone is required to explain the existence of a compressional tectonic regime along the plate interface and the extensional tectonic regime observed at the surface of the seaward slope of the overlying plate (von Huene *et al.* 1998). Events associated with the detachment itself are probably too weak to be detected by the network and are concealed by the high number of aftershocks.

Thermal modelling of the Antofagasta forearc region gives a temperature of 120–150 °C for the upper limit of the seismogenic zone. Within the range of uncertainty, this corresponds to the dehydration of frictionally stable clays to illite and

chlorite, which are more frictionally unstable (Hyndman & Wang 1995). Although sediment coverage is low in the trench axis (Hinz *et al.* 1995), our results may suggest that the dehydration of stable clays controls the upper limit of the seismogenic zone.

## CONCLUSIONS

Applying the concept of the minimum 1-D model results in uniformly precise and reliable hypocentre locations within the network that monitored aftershocks of the 1995 Antofagasta earthquake. Neglecting the individual station elevation in the inversion process yields station corrections that depend both on near-surface heterogeneities beneath the station and on station elevation. By relocating mine blasts, we calculate a mislocation vector of 1 km for the epicentre and 2 km for the focal depth. This mislocation estimate for blasts denotes an upper boundary for deeper events (Kissling 1988). The relatively low mislocation values and the results of stability tests with randomly and systematically shifted hypocentres demonstrate that the minimum 1-D model concept is capable of accurate hypocentre location even in areas of predominantly 2-D structure. Parameters essential for hypocentre accuracy are a suitable distribution of recording stations and the use of *S*-wave arrival times. Reliable hypocentres may only be obtained for events with an azimuthal gap of recording stations of less than 180°, as documented in detail by analysis of the resolution parameters ALE and DSPR introduced by Kradolfer (1989). Hence, without the OBHs, reliable hypocentre determination is restricted to the region within the land-station network.

Precise location of the aftershock series of the large Antofagasta underthrust event (1995 July 30;  $M_w = 8.0$ ) provides a detailed image of the seismogenic zone, where the coupling between the subducting Nazca plate and the overlying South American plate takes place. This seismogenic zone dips at an angle of about 19°–20°, and we determined a depth of 46 km for its lower limit. This agrees well with previously published results inferred from fault plane solutions of locally and teleseismically recorded earthquakes. Since the network incorporated the use of OBHs, we had good control over events located offshore and were able to locate the upper limit of the seismogenic zone at a depth of 20 km. This value is constrained by two other observations: von Huene *et al.* (1998) proposed the existence of a detachment zone above the seismogenic zone to decouple the compressional tectonic regime along the plate interface and the tensional regime at the surface. Numerical modelling of the temperature field of the Antofagasta forearc region (Springer 1997) suggests that dehydration of clays to illites and chlorites, which are more frictionally unstable, may control the upper limit of the seismogenic zone, although sediment coverage is low in the trench axis.

## ACKNOWLEDGMENTS

We wish to thank the SFB 267, the master, crew and scientists of the RV Sonne during legs 2 and 3 of the cruise SO104, and everyone who maintained the stations and pre-processed the data in the field. A. Rietbrock helped us with all questions regarding the GIANT software. M. Sobiesak and R. Patzig helped us with the picking of first arrivals of the large data set. We profited from fruitful discussion with F. Haslinger and

F. Graeber. Most of the plots were generated using the Generic Mapping Tool of Wessel & Smith (1995). The CINCA project is a co-operative research project by the Bundesanstalt für Geowissenschaften und Rohstoffe Hannover, the SFB 267, GEOMAR Kiel, GFZ Potsdam, the Catholic University of the North, Antofagasta, and the University of Chile, Santiago. The CINCA project is funded by the German Federal Ministry for Education, Science, Research and Technology (BMBF) under grant 03G0104. We thank D. Comte, G. Bock, and an anonymous referee for their careful and critical reviews.

## REFERENCES

- Armijo, R. & Thiele, R., 1990. Active faulting in northern Chile, ramp stacking and lateral decoupling along a subduction plate boundary?, *Earth planet. Sci. Lett.*, **98**, 40–61.
- Asch, G., Wylegalla, K., Graeber, F., Haberland, Ch., Rudloff, A., Giese, P. & Wigger, P., 1994. PISCO 94, Proyecto de Investigacion Sismologica de la Cordillera Occidental—Teil 1, Erdbebenregistrierung, *Terra Nova*, **2/94**, 14.
- Asch, G., Bock, G., Graeber, F., Haberland, Ch., Hellweg, M., Kind, R., Rudloff, A. & Wylegalla, K., 1995. Passive Seismologie im Rahmen von PISCO'94, *Report of the SFB 267 'Deformation processes in the Andes'*, pp. 619–667, Berlin.
- Byrne, D.E., Davis, D.M. & Sykes, L.R., 1988. Loci and maximum size of the thrust earthquakes and the mechanics of the shallow region of subduction zones, *Tectonics*, **7**, 833–857.
- Comte, D. & Suarez, G., 1995. Stress distribution and geometry of the subducting Nazca plate in northern Chile using teleseismically recorded earthquakes, *Geophys. J. Int.*, **122**, 419–440.
- Comte, D., Pardo, M., Dorbath, L., Dorbath, C., Haessler, H., Rivera, L., Cisterna, A. & Ponce, L., 1994. Determination of seimogenic interplate contact zone and crustal seismicity around Antofagasta, northern Chile using local data, *Geophys. J. Int.*, **116**, 553–561.
- Crosson, R.S., 1976. Crustal structure modeling of earthquake data, 1, Simultaneous least squares estimation of hypocenter and velocity parameters, *J. geophys. Res.*, **81**, 3036–3046.
- Delouis, B., Cisternas, A., Dorbath, L., Rivera, L. & Kausel, E., 1996. The Andean subduction zone between 22 and 25° S (northern Chile): precise geometry and state of stress, *Tectonophysics*, **259**, 81–100.
- Delouis, B., Monfret, T., Dorbath, L., Pardo, M., Rivera, L., Comte, D., Haessler, H., Caminade, J.P., Ponce, L., Kausel, E. & Cisternas, A., 1997. The Mw = 8.0 Antofagasta (northern Chile) earthquake of 30 July 1995: a precursor to the end of the large 1877 gap, *Bull. seism. Soc. Am.*, **87**, 427–445.
- Delouis, B., Philip, H., Dorbath, L. & Cisternas, A., 1998. Recent crustal deformation in the Antofagasta region (northern Chile) and the subduction process, *Geophys. J. Int.*, **132**, 302–338.
- Eberhart-Phillips, D. & Michael, A.J., 1993. Three-dimensional velocity structure, seismicity, and fault structure in the Parkfield region, central California, *J. geophys. Res.*, **98**, 737–758.
- Gomberg, J.S., Shedlock, K.M. & Roecker, S.W., 1990. The effect of S-wave arrival times on the accuracy of the hypocenter estimation, *Bull. seism. Soc. Am.*, **80**, 1605–1628.
- Graeber, F., 1997. Seismische Geschwindigkeiten und Hypozentren in den südlichen zentralen Anden aus der simultanen Inversion von Laufzeitdaten des seismologischen Experiments PISCO'94 in Nordchile, *Scientific Technical Report STR97/17*, GeoForschungszentrum, Potsdam.
- Hinz, K. *et al.*, 1995. Crustal investigations off- and onshore Nazca/Central Andes, CINCA, Sonne Cruise 104, Leg 1, 22.07.–24.08. 1995, Bundesanstalt für Geowissenschaften und Rohstoffe, Hannover, Archiv-Nr. BGR 113.998, Tagebuch-Nr. 12. 192/95.
- Hyndman, R.D. & Wang, K., 1995. The rupture zone of Cascadia great earthquakes from current deformation and thermal regime, *J. geophys. Res.*, **100**, 22 133–22 154.
- Kissling, E., 1988. Geotomography with local earthquakes, *Rev. Geophys.*, **26**, 659–698.
- Kissling, E. & Lahr, J.C., 1991. Tomographic image of the Pacific Slab under southern Alaska, *Ecolgae geol. Helv.*, **84/2**, 297–315.
- Kissling, E., Ellsworth, W.L., Eberhart-Phillips, D. & Kradolfer, U., 1994. Initial reference models in local earthquake tomography, *J. geophys. Res.*, **99**, 19 635–19 646.
- Kissling, E., Kradolfer, U. & Maurer, H., 1995a. *VELEST User's Guide – Short Introduction*, Institute of geophysics and Swiss seismological service, ETH, Zurich.
- Kissling, E., Solarino, S. & Cattaneo, M., 1995b. Improved seismic velocity reference model from local earthquake data in Northwestern Italy, *Terra Nova*, **7**, 528–534.
- Kradolfer, U., 1989. Seismische Tomographie in der Schweiz mittels lokaler Erdbeben, *Phd thesis*, ETH, Zürich.
- Maurer, H. & Kradolfer, U., 1996. Hypocentral parameters and velocity estimation in the western Swiss alps by simultaneous inversion of P- and S-wave data, *Bull. seism. Soc. Am.*, **86**, 32–42.
- Menke, W., 1984. *Geophysical Data Analysis: Discrete Inverse Theory*, Academic Press, San Diego.
- Pacheco, J.F., Sykes, L.R. & Scholz, C.H., 1993. Nature of seismic coupling along simple plate boundaries of the subduction type, *J. geophys. Res.*, **98**, 14 133–14 159.
- Rietbrock, A. & Scherbaum, F., 1998. The GIANT analysis system (graphical interactive aftershock network toolbox), *Seism. Res. Lett.*, **69**, 40–45.
- Ruff, L., 1996. Large earthquakes in subduction zones: segment interaction and recurrence time, in *Subduction: Top to Bottom*, pp. 91–105, eds Bebout, G.E., Scholl, D.W., Kirby, S.H. & Platt, P., Geophysical Monograph 96, AGU.
- Ruff, L. & Tichelaar, B., 1996. What controls the seismogenic plate interface in subduction zones, in *Subduction: Top to Bottom*, pp. 105–1013, eds Bebout, G.E., Scholl, D.W., Kirby, S.H. & Platt, P., Geophysical Monograph 96, AGU.
- Scheuber, E., Bogdanic, T., Jensen, A. & Reutter, K.-J., 1994. Tectonic development of the North Chilean Andes in relation to plate convergence and magmatism since the Jurassic, in *Tectonics of the Southern Central Andes*, pp. 121–139, eds Reutter, K.-J., Scheuber, E. & Wigger, P.-J., Springer Verlag, Berlin.
- Solarino, S., Kissling, E., Cattaneo, M. & Eva, C., 1997. Local earthquake tomography of the southern part of the Ivrea body, North-Western Italy, *Ecolgae geol. Helv.*, **90**, 357–364.
- Springer, M., 1997. Die Oberflächenwärmefludichte-Verteilung in den zentralen Anden und daraus abgeleitete Temperaturmodelle der Lithosphäre, *PhD thesis*, FU-Berlin.
- Thurber, C.H., 1992. Hypocenter-velocity structure coupling in local earthquake tomography, *Phys. Earth planet. Inter.*, **75**, 55–62.
- Tichelaar, B. & Ruff, L., 1991. Seismic coupling along the Chilean subduction zone, *J. geophys. Res.*, **96**, 11 997–12 022.
- Tichelaar, B. & Ruff, L., 1993. Depth of seismic coupling along subduction zones, *J. geophys. Res.*, **98**, 2017–2037.
- von Huene, R. & Scholl, D.W., 1991. Observations at convergent margins concerning sediment subduction, subduction erosion and the growth of continental crust, *Rev. Geophys.*, **29**, 279–316.
- von Huene, R., Weinrebe, W. & Heeren, F., 1999. Subduction erosion along the north Chilean margin, *J. Geodyn.*, **27**, 345–358.
- Wessel, P. & Smith, W.H.F., 1995. New version of the Generic Mapping Tool released, *EOS, Trans. Am. geophys. Un.*, **76**, 329.
- Wiens, D., 1989. Bathymetric effects on body waveforms from shallow subduction earthquakes and application to seismic processes in the Kuril Trench, *J. geophys. Res.*, **98**, 2955–2972.
- Wigger, P.J., Schmitz, M., Araneda, M., Asc, G.H., Baldzuhn, P., Giese, P., Heinsohn, W.-D., Martinez, E., Ricaldi, E., Röwer, P. & Viramonte, J., 1994. Variation in the crustal structure of the Southern Central Andes deduced from seismic refraction investigation, in *Tectonics of the Southern Central Andes*, pp. 23–48, eds Reutter, K.-J., Scheuber, E. & Wigger, P.-J., Springer Verlag, Berlin.